

# P-wave monitoring of hydrate-bearing sand during CH<sub>4</sub>–CO<sub>2</sub> replacement

D. Nicolas Espinoza\*, J. Carlos Santamarina

School of Civil and Environmental Engineering, Georgia Institute of Technology, 790 Atlantic Drive, Atlanta, GA 30332-0355, USA

## ARTICLE INFO

### Article history:

Received 31 August 2010  
Received in revised form 8 February 2011  
Accepted 11 February 2011  
Available online 24 March 2011

### Keywords:

Natural gas enhanced recovery  
Carbon geological storage  
Reservoir  
Geomechanics  
Geophysics  
Gas exchange

## ABSTRACT

The replacement of methane for carbon dioxide in natural gas hydrate-bearing sediments is a promising technology in view of a more sustainable use of fossil fuels. While previous studies have shown successful CH<sub>4</sub>–CO<sub>2</sub> replacement in hydrates, the mechanical response of hydrate-bearing sediments during CO<sub>2</sub> injection, CH<sub>4</sub>–CO<sub>2</sub> replacement, and CH<sub>4</sub> production needs to be adequately understood in order to avert production problems such as borehole instability, sand production, and buckling of the casing. We take advantage of the characteristics of elastic mechanical wave propagation in sediments to monitor CH<sub>4</sub> hydrate-bearing sands before, during, and after CO<sub>2</sub> injection. Results show that CH<sub>4</sub>–CO<sub>2</sub> replacement occurs without a loss of stiffness in the granular medium. This implies that CO<sub>2</sub>-flooded sandy reservoirs can remain mechanically stable during and after CH<sub>4</sub> gas production. On the other hand, dry CO<sub>2</sub> dissolves hydrate, and continued sediment flushing with dry CO<sub>2</sub> reduces the degree of hydrate saturation in the pore space, opens the pore throats, and weakens the granular skeleton. This phenomenon may cause a significant loss of strength near the injection points and regions subjected to high liquid CO<sub>2</sub> flow rate. The results of complimentary analyses show a decrease in bulk stiffness as water is displaced by liquid CO<sub>2</sub>, a stiffening of the granular skeleton during hydrate formation at contacts (diffusion limited), and the implications of water solubility in liquid CO<sub>2</sub>.

© 2011 Elsevier Ltd. All rights reserved.

## 1. Introduction

The simultaneous injection and geological entrapment of CO<sub>2</sub>, along with enhanced hydrocarbon recovery may increase the efficiency and sustainability of fossil fuels. Examples of these combined processes are CO<sub>2</sub> enhanced oil recovery, and CO<sub>2</sub> enhanced coal bed methane recovery. In this study, we focus on CH<sub>4</sub>–CO<sub>2</sub> hydrate replacement whereby methane is recovered from hydrate-bearing sediments with the concurrent entrapment of CO<sub>2</sub>.

Published theoretical studies and laboratory-scale experiments have shown the successful release of CH<sub>4</sub> as a result of the replacement reaction caused by CO<sub>2</sub> injection (Hirohama et al., 1996; Kvamme et al., 2007; Lee et al., 2003; McGrail et al., 2007; Tegze et al., 2007). Pore scale phenomena include heat release and diffusion controlled reactions, dissolution of fluid phases, gas production, and porefluid volume expansion (note: a comprehensive review of phenomena relevant to CH<sub>4</sub>–CO<sub>2</sub> replacement can be found in Jung et al. (2010)). The first reservoir-scale trial test has been planned for the Alaska North Slope in 2011 (DOE – project DE-NT0006553).

P-waves provide insight into the stiffness evolution of hydrate-bearing sediments. The stiffness evolution affects the mechanical

stability of production wellbores and gas hydrate reservoirs. P-wave methods have been used to monitor CO<sub>2</sub> field injection tests (Arts et al., 2004; Daley et al., 2008; James et al., 1995; Spyros and Bruce, 1997; Spyros et al., 1995; Xue et al., 2006) and to assess CO<sub>2</sub> transport and saturation in laboratory experiments (Angeli et al., 2009; Lei and Xue, 2009; Sarout et al., 2009; Shi et al., 2007). In this study we use P-waves to monitor the evolution of CH<sub>4</sub> hydrate formation, CO<sub>2</sub> flooding, CH<sub>4</sub>–CO<sub>2</sub> replacement, and final hydrate dissociation in sands. The properties of CO<sub>2</sub> and CH<sub>4</sub> are reviewed first. This is followed by the experimental study and complimentary analyses.

## 2. Review of CO<sub>2</sub> and CH<sub>4</sub> properties

The physical and chemical properties of CO<sub>2</sub> depend on pressure–temperature PT conditions. The critical point of CO<sub>2</sub> is at  $P=7.38$  MPa and  $T=304.1$  K. The density of liquid CO<sub>2</sub> is usually lower than that of water, but there may be a density reversal at high pressure, such as in deep-sea settings (at 277.15 K,  $\rho_{\text{CO}_2} > 1035$  kg/m<sup>3</sup> when pressure is above ~28 MPa). The bulk compressibility of liquid CO<sub>2</sub> is an order of magnitude higher than that of water (Span and Wagner, 1996). The most important properties of CO<sub>2</sub> relevant to transport-conduction processes are: (a) very low viscosity, typically 10 times lower than that of water ( $\mu_{\text{CO}_2} = 10^{-4}$  Pa s at 10 MPa and 280 K – Fenghour et al., 1998); (b) high diffusivity of water into liquid CO<sub>2</sub> ( $D \approx 2\text{--}20 \times 10^{-8}$  m<sup>2</sup>/s at

\* Corresponding author.

E-mail address: [nicolas@ce.gatech.edu](mailto:nicolas@ce.gatech.edu) (D.N. Espinoza).

**Table 1**  
Physical and mechanical properties of hydrate-bearing sediment constituents. The following constants and equations are used to predict P-wave velocity for the multiphase fluid-sediment system using the Biot–Gassman equation (Eqs. (3) and (4)).

Phase	CO <sub>2</sub>	CH <sub>4</sub>	Water-brine	Ice	Gas Hydrate	Mineral
<i>Physical properties</i>						
Mass density, $\rho$ (kg/m <sup>3</sup> )	CO <sub>2</sub> EOS <sup>a</sup>	CH <sub>4</sub> Peng–Robinson EOS <sup>b</sup>	Correlation <sup>c</sup>	921 <sup>d</sup>	CH <sub>4</sub> hyd: 930 <sup>e</sup> CO <sub>2</sub> hyd: 1100 <sup>f</sup>	Quartz: 2650
Viscosity, $\mu$ (Pa s)	Experimental fitting <sup>g</sup>	$2 \pm 0.5 \times 10^{-5}$ h	$\sim 1.5 \times 10^{-3}$ i	Does not apply	Does not apply	Does not apply
<i>Mechanical properties</i>						
P-wave velocity, $V_p$ (m/s)	Correlation based on <sup>j</sup>	Polynomial equation <sup>k</sup>	Equation <sup>l</sup>	3870 <sup>d</sup>	3780 <sup>d</sup>	6060 <sup>m</sup>
S-wave velocity, $V_s$ (m/s)	0	0	0	1949 <sup>d</sup>	1963 <sup>d</sup>	4110 <sup>m</sup>
Shear modulus, $G$ (GPa)	0	0	0	3.45 <sup>d</sup>	3.2 <sup>n</sup> 3.54 <sup>d</sup>	45 <sup>i</sup>
Bulk modulus, $B$ (GPa)	$f(V_p, \rho)$ †	$f(V_p, \rho)$ †	$f(V_p, \rho)$ †	9.18 <sup>d</sup>	7.1 <sup>m</sup> 8.51 <sup>d</sup>	37 <sup>i</sup>
Poisson ratio, $\nu$	$\sim 0.5$	$\sim 0.5$	$\sim 0.5$	0.33 <sup>d</sup>	0.32 <sup>d</sup>	$\sim 0.08$ <sup>m</sup>

<sup>a</sup> Duan and Sun (2003).

<sup>b</sup> Peng–Robinson parameters:  $T_c = 191.15$  K,  $P_c = 4.641$  MPa,  $\omega = 0.0115$ .

<sup>c</sup> Mavko et al. (2009).

<sup>d</sup> 31 MPa effective stress and 273.15 K (Helgerud et al., 2009).

<sup>e</sup> Sloan and Koh (2008).

<sup>f</sup> Aya et al. (1997).

<sup>g</sup> Fenghour et al. (1998) and Vesovic et al. (1990).

<sup>h</sup> At 298 K, 10–20 MPa (Bicher and Katz, 1943).

<sup>i</sup> Brine at 293 K (Netherton et al., 1977).

<sup>j</sup> Span and Wagner (1996).

<sup>k</sup> Trusler and Zarari (1992).

<sup>l</sup> Belogol'skii et al. (2002) and Mavko et al. (2009).

<sup>m</sup> Gueguen and Palciauskas (1994).

† Computed value.

7–20 MPa and  $\sim 300$  K – Espinoza and Santamarina, 2010), (c) significant solubility of water in liquid CO<sub>2</sub> (0.05 mol/kg at 10 MPa and 285 K – Spycher et al., 2003), and (f) high solubility of CO<sub>2</sub> in water (0.83 mol/kg at 6.6 MPa and 274 K in the presence of hydrate – Hashemi et al., 2006).

The critical point of CH<sub>4</sub> is at  $P = 4.60$  MPa and  $T = 190.6$  K, therefore, CH<sub>4</sub> does not form as a liquid phase in geological reservoir applications. The mass density of gas CH<sub>4</sub> can be approximated with a cubic equation of state (see parameters in Table 1 – Peng and Robinson, 1976). The mass density and viscosity of CH<sub>4</sub> are low at reservoir conditions when compared to water; for example,  $\rho_{\text{CH}_4} = 232$  kg/m<sup>3</sup> and  $\mu_{\text{CH}_4} = 2.7 \times 10^{-5}$  Pa s at  $P = 30$  MPa and  $T = 280$  K (NIST, 2010).

Both, CO<sub>2</sub> and CH<sub>4</sub> can form gas hydrates at high pressure and low temperature. Water molecules form a polyhedral structure, which allows them to host the corresponding gas molecules (Sloan and Koh, 2008). Even though both CO<sub>2</sub> and CH<sub>4</sub> form hydrate structure I, their solubility in water, cage occupancy in the hydrate, and thermodynamic stability inside hydrate cages differ significantly (Adisasmito et al., 1991; Anderson et al., 2003; Servio and Englezos, 2001, 2002). Mixed CH<sub>4</sub>–CO<sub>2</sub> gas conditions cause a shift in stability boundaries which depends on the CH<sub>4</sub>/CO<sub>2</sub> mass ratio (Adisasmito et al., 1991; Seo and Lee, 2001).

Gas hydrates form in the pore space of sediments at the bottom of the ocean and at great depths in permafrost where  $PT$  conditions are within the hydrate stability zone and CH<sub>4</sub> is abundant (Kvenvolden, 1988). The pore habit of hydrates in sediments has a large impact on the physical properties of hydrate-bearing sediments (e.g. pore filling, segregated lenses, and cementing – Waite et al., 2009).

### 3. Design of experiments

We use P-waves to assess the evolution of hydrate in sediments. We purposely localize hydrate growth at contacts by using a partially saturated sand pack, so that all of the water is found

at interparticle menisci. Therefore, the granular medium acts as a “sensor” that amplifies the signature of the physical processes taking place at tens of thousands of grain contacts. In particular, sand grains work as Hertzian stiffness sensors that can reflect minor changes in contact conditions. Thus, compressive and shear wave velocities increase significantly even with small changes in hydrate saturation (note: hydrate nucleates on grain surfaces and grows into the pore in water saturated sediments; much lower changes in stiffness take place in this case).

#### 3.1. Materials

Ottawa Sand #20/30 is the host sediment (round grains,  $d_{50} = 0.72$  mm and  $d_{60}/d_{10} = 1.2$ , where  $d_x$  is the diameter for the  $x$ -percentile in the distribution – details in Cho et al. (2006)). Fluids include research purity CO<sub>2</sub> and CH<sub>4</sub> gases, and distilled water.

#### 3.2. Apparatus

The tests are conducted within a high-pressure chamber equipped with multiple ports for fluid injection, electronics connections, and pressure measurement devices (transducer Omega PX303-GV). A sapphire window allows for direct observation into the pressure chamber. Inside the chamber, we place a spring-loaded sediment cell (25 mm diameter and  $\sim 20$  mm height – Fig. 1) designed to apply a 100 kPa effective axial stress at zero lateral strain conditions. The cell is equipped with piezoelectric transducers (5 mm radius, 0.2 mm thickness) to generate and receive P-waves (Fig. 1). The piezoelectric transducers are connected to a signal generator BK PRECISION 4012A and an oscilloscope HP54600B. The input signal is a step function that repeats every 20 ms. The output signal is passed through a 300 kHz low-pass analogue filter and is sampled at 5 MHz. A total of 32 consecutive signals are averaged to increase the signal-to-noise ratio, and stored every 30 s (note: we observe the waveforms on the oscilloscope screen continuously during critical processes). A thermocouple

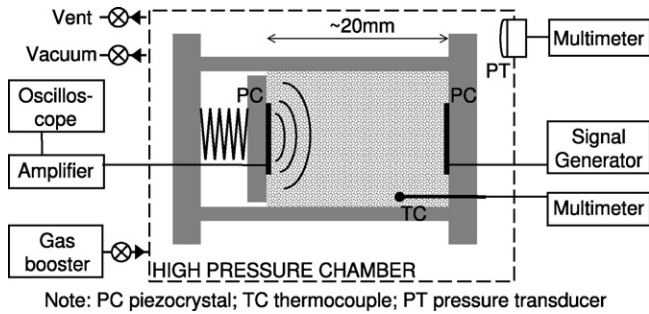


**Fig. 1.** Experimental devices. The spring-loaded sediment cell is housed inside the pressure chamber (shown with a dashed line). The spring applies a constant effective axial stress  $\sigma' \approx 100$  kPa to the sand. The piezoelectric transducers attached to the lower and upper plates of the cell are used to generate and measure the compressive P-waves. A thermocouple (bottom right corner in the cell) measures the sediment temperature.

(Copper Constantan, Conax Buffalo) placed inside the sediment cell measures the pore-fluid temperature within the sand specimen. The sediment cell is perforated (0.5 mm diameter holes) to retain the sand grains and but to allow the free flow of  $\text{CH}_4$  and  $\text{CO}_2$ .

### 3.3. Experimental procedure

The sand is mixed with distilled water, packed inside the sediment cell, and loaded to a constant effective axial stress. Then, we place the sediment cell inside the pressure chamber, briefly apply a partial vacuum, and flush the system with  $\text{CH}_4$  gas at least five times in order to remove the air inside of the chamber and specimen pore space. Immediately after, we start to log pressure, temperature, and P-wave arrivals.

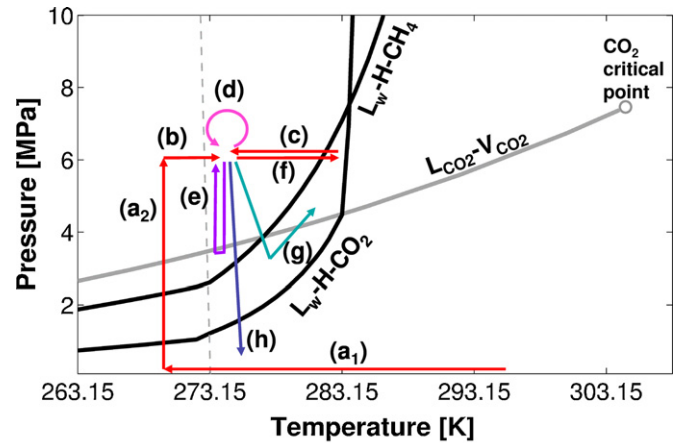
We run a total of seven multi-stage tests using the same sand, at the same effective stress, but with different initial values of water saturation. We subject each specimen to a pre-specified pressure–temperature PT time history to gain detailed information related to hydrate formation,  $\text{CH}_4$ – $\text{CO}_2$  replacement, and subsequent dissociation. Ice and hydrate formation PT paths are chosen to facilitate hydrate formation and to gain physical insight. The PT histories during  $\text{CO}_2$  flooding represent two plausible scenarios: (a) flooding inside the  $\text{CH}_4$  hydrate stability field is expected to be safer but slower, while (b)  $\text{CO}_2$  gas injection coupled with depressurization may be quicker but may be accompanied by sediment compaction. PT paths that induce hydrate dissociation allow us to confirm PT conditions at phase transition for either  $\text{CO}_2$  or  $\text{CH}_4$  hydrate. Finally, successive  $\text{CO}_2$  flushing is relevant to anticipate the response of hydrate-bearing sediments subjected to high  $\text{CO}_2$  advection. Results are summarized in the following section.

## 4. Results

The main stages in the various PT time histories are shown in Fig. 2. Fig. 3 shows typical waveform cascades measured during the different stages. The dominant frequency of the transducer–sediment coupled system is in the ultrasonic regime and ranges from  $\sim 20$  kHz (sand pack in air) to 150 kHz (cemented by ice or hydrate). Specific observations for each PT stage are summarized next.

### 4.1. Ice and hydrate formation

(a) Specimen cooling and ice formation at grain contacts (path  $a_1$  in Fig. 2). Ice formation lasts from 30 to 350 s for water saturation  $S_w = 0.045$  to 0.37 (exothermic-heat transport controlled).



- |   |  |
|---|--|
| (a) Freezing and pressurization                     | (e) $\text{CO}_2$ liquid-gas-liquid cycle            |
| (b) $\text{CH}_4$ hydrate formation from ice        | (f) $\text{CH}_4$ hydrate dissociation               |
| (c) $\text{CH}_4$ hydrate formation from water      | (g) $\text{CO}_2$ flooding outside $\text{CH}_4$ HSZ |
| (d) $\text{CO}_2$ flooding inside $\text{CH}_4$ HSZ | (h) Depressurization - Dissociation                  |

**Fig. 2.** Pressure–temperature time histories. The arrows show the PT conditions followed in various tests, not necessarily in chronological order (letters match datasets in Fig. 3). Phase boundaries are shown for  $\text{CH}_4$  and  $\text{CO}_2$  hydrate, the liquid–vapor boundary for pure  $\text{CO}_2$  and the water–ice boundary as a dashed line (equations in Jung et al. (2010)). Initially, we freeze the water in a  $\text{CH}_4$  atmosphere ( $a_1$ ) and then increase pressure by injecting  $\text{CH}_4$  gas ( $a_2$ ). We formed hydrate from ice to hydrate (b) and from liquid water (c).  $\text{CO}_2$  injection is shown as loops, first  $\text{CO}_2$  flooding (d), followed by liquid–gas–liquid  $\text{CO}_2$  cycles (e). The  $\text{CH}_4$ – $\text{CO}_2$  replacement is sought during the first  $\text{CO}_2$  flooding inside the  $\text{CH}_4$  HSZ (d) or during the excursion outside the  $\text{CH}_4$  hydrate stability field (g). We dissociate any hydrate during the final depressurization step (h).

A pronounced increase in stiffness accompanies ice formation (e.g. Fig. 3a, initial  $S_w = 0.045$ ).

- (b)  $\text{CH}_4$  hydrate formation from ice in an excess- $\text{CH}_4$  atmosphere (paths  $a_2$  and b in Fig. 2). The ice-bearing sediment is pressurized with  $\text{CH}_4$  (path  $a_2$ ) and warmed outside of the ice stability field (path b). We observe that  $\text{CH}_4$  hydrate nucleates as ice melts. While hydrate formation at each meniscus is  $\text{CH}_4$  diffusion-limited, the volume average P-wave velocity remains higher than in the unfrozen sediment at all times (Fig. 3b is a continuation of Fig. 3a – initial  $S_w = 0.045$ ). Hydrate continues growing for  $\sim 12$  h and the sediment mixture continues to increase in stiffness (only 45 min shown in Fig. 3b).
- (c)  $\text{CH}_4$  hydrate formation from water in an excess- $\text{CH}_4$  atmosphere (path c in Fig. 2). In this case, the initial sediment temperature is above that of the hydrate phase boundary, and the hydrate is formed by cooling (Fig. 3c). This process is much longer than ice formation because the growth is not governed by heat transfer but instead by the  $\text{CH}_4$  diffusive transport through the hydrate layer that forms at the interface between the penular water and the bulk  $\text{CH}_4$  gas (for  $S_w = 0.10$ , ice formation takes place in less than 30 s, yet hydrate formation requires about 24 h). The duration of hydrate formation increases with the initial water saturation  $S_w$ .

### 4.2. $\text{CO}_2$ flooding

- (d)  $\text{CO}_2$  flooding and displacement of  $\text{CH}_4$  (path d in Fig. 2). After  $\text{CH}_4$  hydrate forms at grain contacts, we flood the pore space with gaseous, then, liquid  $\text{CO}_2$  while the PT conditions remain within the  $\text{CH}_4$  hydrate stability field.  $\text{CH}_4$  is slowly vented while  $\text{CO}_2$  is pumped into the chamber. The liquid phase formation is observed through the sapphire window; the interface rises to eventually fill the chamber as the injection of  $\text{CO}_2$  continues. From PT conditions and bubble point data, we estimate that less than 10% of the methane remained in the chamber,

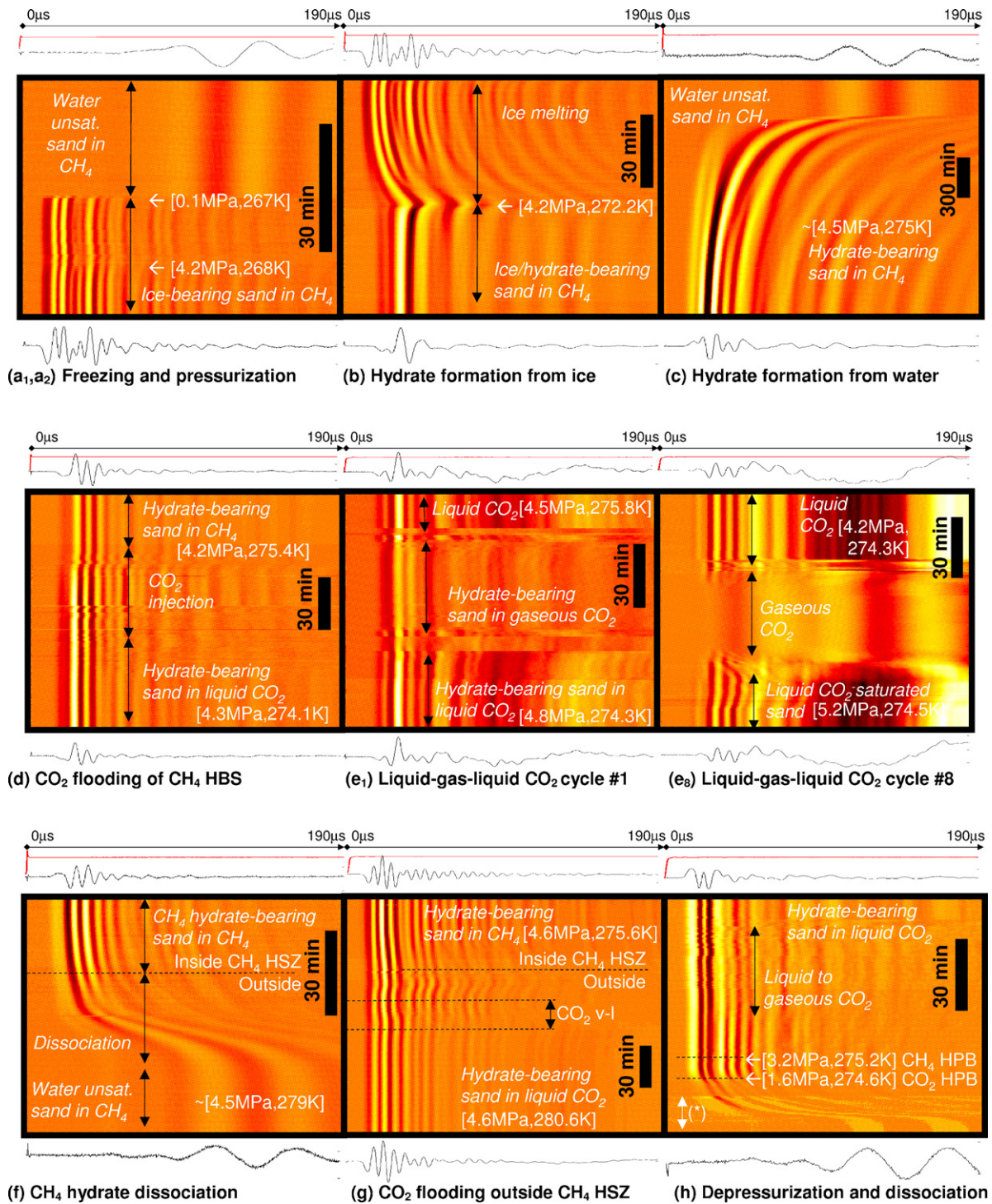


**Fig. 3.** P-wave measurements in hydrate-bearing sand (void ratio  $e \sim 0.7$ , effective confining stress  $\sigma' \sim 100$  kPa, and mean particle size  $d_{50} = 0.72$  mm). Waveforms from time-lapse P-wave monitoring: x-axis, oscilloscope time ( $\mu$ s); y-axis, experimental time from the top to the bottom (min). Waveform voltage in colors, white denotes the signal peaks and black the signal troughs. Each frame represents a different process (results from various tests – refer to Fig. 2 and Section 3). Notice the high contrast in frequency and amplitude between water unsaturated and either ice or hydrate-bearing sediments. Notes: HPB hydrate phase boundary, \* increased contrast to show low amplitude waveforms. Summary of PT histories for experiments shown in this figure: (1) initial  $S_w = 0.045$  (a<sub>1</sub>, a<sub>2</sub>, b, d, e, and h); (2) initial  $S_w = 0.10$  (a<sub>1</sub>, a<sub>2</sub>, b, f, c, d, h); and (3) initial  $S_w = 0.27$  (a<sub>1</sub>, a<sub>2</sub>, b, f, c, g, and final depressurization).

mostly above the sediment cell (see CH<sub>4</sub>–CO<sub>2</sub> phase equilibria in Donnelly and Katz, 1954). Fig. 3d shows the results gathered during the liquid CO<sub>2</sub> flooding of a CH<sub>4</sub> hydrate-bearing sand at a hydrate saturation of  $S_{hyd} \sim 0.045$ ; based on the evolution of P-wave velocity to an asymptotic value and on the time for diffusion-controlled growth (Section 5.3), we assume all water

has converted to hydrate at this point. PT conditions remain within the CH<sub>4</sub> hydrate stability field. There is no significant stiffness change.

(e) Liquid–gas–liquid CO<sub>2</sub> cycle at  $S_{hyd} \sim 0.045$  (path e in Fig. 2). We renew the CO<sub>2</sub> in the pore space by imposing a liquid–gas–liquid CO<sub>2</sub> cycle, to simulate extensive flushing of the sediment with

pure liquid CO<sub>2</sub>. Fig. 3e<sub>1</sub> shows the first of ten CO<sub>2</sub> flushing cycles. The wave velocity does not change significantly when the pore-fluid is changed from liquid CO<sub>2</sub> to gaseous CO<sub>2</sub>.

- (f) Liquid–gas–liquid CO<sub>2</sub> cycle at  $S_{hyd} \ll 0.045$  (same as path e in Fig. 2). When hydrate saturation is very low, the difference in bulk stiffness when pores are filled with liquid CO<sub>2</sub>, as opposed to gaseous CO<sub>2</sub>, is evident (Fig. 3e<sub>8</sub>): as soon as CO<sub>2</sub> vaporizes, the waveform shifts to having long travel time ( $\sim 20 \mu\text{s}$  to  $>40 \mu\text{s}$ ) and low frequency.

#### 4.3. Hydrate dissociation

- (f) Dissociation of CH<sub>4</sub> hydrate (path f in Fig. 2). Fig. 3f shows CH<sub>4</sub> hydrate-bearing sand in CH<sub>4</sub> gas as it is heated beyond the hydrate stability field. The dissociation of CH<sub>4</sub> hydrate takes  $\sim 20$  min for initial  $S_{hyd} \sim 0.10$  (Fig. 3f). As soon as the specimen crosses the CH<sub>4</sub> hydrate dissociation boundary, the P-wave velocity starts to decrease. After complete dissociation, the effective stress acting on the granular skeleton dominates the sediment stiffness (note: Fig. 3c is a continuation of Fig. 3f).
- (g) Dissociation of CH<sub>4</sub> hydrate in the presence of CO<sub>2</sub> (path g in Fig. 2). In this experiment, we take a specimen of CH<sub>4</sub> hydrate-bearing sand in CH<sub>4</sub> gas beyond the CH<sub>4</sub> hydrate stability field and simultaneously inject CO<sub>2</sub> in order to reach the region bound by the CH<sub>4</sub> and CO<sub>2</sub> hydrate phase boundaries. Upon continued CO<sub>2</sub> injection, the CO<sub>2</sub> gas becomes liquid CO<sub>2</sub>. From PT conditions and dew point data, we estimate that less than 10% methane stayed in the chamber, mostly above the sediment cell (see CH<sub>4</sub>–CO<sub>2</sub> phase equilibria in Donnelly and Katz (1954)). The P-wave velocity hardly changes during the process (Fig. 3g,  $S_{hyd} = 0.27$ , during the time shown and afterwards). We observe this “hydrate preservation behavior” at low hydrate saturation as well ( $S_{hyd} = 0.03$  – not shown in Fig. 3).
- (h) Hydrate dissociation after CO<sub>2</sub> flooding (path h in Fig. 2). Fig. 3h shows the dissociation of originally pure CH<sub>4</sub> hydrate in sand ( $S_{hyd} \sim 0.10$ )  $\sim 48$  h after the injection of liquid CO<sub>2</sub>. During depressurization, the specimen goes through the CH<sub>4</sub> hydrate phase boundary first; but the P-wave velocity remains almost constant until the CO<sub>2</sub> hydrate phase boundary is reached. A rapid loss of stiffness occurs once the PT conditions are beyond the CO<sub>2</sub> hydrate stability field, and the sediment stiffness returns to the original water-wet condition. Complete dissociation lasts  $\sim 15$  min.

#### 4.4. CO<sub>2</sub> flushing

We flush the CO<sub>2</sub> in the sediment by imposing the CO<sub>2</sub> pressure cycles sketched as path e in Fig. 2. Fig. 4 shows the complete stiffness evolution for a hydrate-bearing sand ( $S_{hyd} \sim 0.045$ ) subjected to ten CO<sub>2</sub> flushing cycles (note: this is a 35 day long experiment; ice formation, hydrate formation from ice, and CH<sub>4</sub> displacement by liquid CO<sub>2</sub> are shown for completeness). The granular skeleton stiffness decreases gradually with each CO<sub>2</sub> flushing cycle. The P-wave velocity at the eighth flushing cycle is the same as for the water-wet sand pack at 100 kPa. We dismantled the chamber and recovered only dry sand from the sediment cell.

### 5. Complimentary analyses and discussion

Earlier physico-chemical arguments at the lattice-scale suggested that a solid–liquid–solid transition is required for CH<sub>4</sub>–CO<sub>2</sub> replacement (Jung et al., 2010). However, macroscale experimental results presented here show almost constant sediment stiffness during CH<sub>4</sub>–CO<sub>2</sub> replacement. It is concluded that the solid–liquid–solid transition takes place locally at a scale small

enough that the sediment volume average properties remain unchanged. Clearly, hydrate dissolution in liquid CO<sub>2</sub>-saturated reservoirs will be accompanied by stiffness loss (e.g. near the injection well), while new hydrate formation in excess-water reservoirs will increase the sediment stiffness (typically in the far field of the injection well).

The following complimentary analyses permit extracting additional information from these experiments and provide an approach to assess changes in the geological formation.

#### 5.1. Frequency effects

The piezoelectric transducers used in this study have a high resonant frequency in air. Once buried in the sand, the resonant frequency is strongly dependent on the sand stiffness and the sediment mass within the near field of the transducer. Assuming a parallel stiffness model, we can estimate the effective natural frequency of the coupled sand-transducer system  $f_c$  (underlying expressions in Bevlins (1979); an analogous analysis for buried bender elements can be found in Lee and Santamarina (2005)).

$$f_c \approx \frac{1}{2\pi} \sqrt{\frac{(70^2/3)(t/r)^3(E_p/(1-\nu_p^2)) + \eta E_s}{[(t/r)\rho_p + \beta\rho_s]\pi r^2}} \quad (1)$$

where  $\beta = 2$  (first mode of vibration) and  $\eta \sim 1.6$  (Poulos and Davis, 1974) are geometry related factors, and  $E_p$  and  $\nu_p$  are the Young's modulus and Poisson's ratio of the transducer. The sediment stiffness  $E_s$  determines the resonant frequency of these buried, thin transducers (thickness much smaller than the radius,  $t/r \ll 1$ ). Indeed, experimental results show that at an effective stress of  $\sigma' \sim 100$  kPa, the dominant spectral frequency ranges from 20 kHz (sediment without ice or hydrate) to 150 kHz (sediment with ice or hydrate). These values are readily corroborated by time series shown in Fig. 3. In all cases, the wavelength  $\lambda$  is greater than 20 times the grain size  $d_{50}$  and satisfies the equivalent continuum assumption. The wavelength  $\lambda$  remains significantly shorter than the travel distance in all measurements.

The frequency content of P-waves in the sand saturated with liquid CO<sub>2</sub> (refer to Fig. 3) often exceeds Biot's characteristic frequency (Biot, 1956) for our experimental conditions ( $\phi \sim 0.42$ ,  $\mu_{\text{liquid CO}_2} \sim 10^{-4}$  Pa s,  $\rho_{\text{liquid CO}_2} \sim 0.9$  kg/m<sup>3</sup>, and  $\kappa \sim 10^{-12}$  m<sup>2</sup>).

$$f_c = \frac{\phi \mu_{\text{CO}_2}}{2\pi \rho_{\text{CO}_2} \kappa} \sim 10 \text{ kHz} \quad (2)$$

The ratio between the high and low frequency P-wave velocity is  $\sim 1.07$  (equation in Santamarina et al. (2001)) and has a minor effect in these results and analysis. In view of field applications, we continue the analysis of P-wave velocity for the low frequency regime.

#### 5.2. P-wave velocity – changes during liquid CO<sub>2</sub> flooding

In the low-frequency regime, the mixture bulk compressibility  $B_{mix}$  can be estimated using the low frequency Biot–Gassman equation (Bourbie et al., 1987; Mavko et al., 2009), while the mixture mass density  $\rho_{mix}$  is computed as a volume average. The general expressions for the system under consideration are,

$$B_{mix} = B_{sk} + \left(1 - \frac{B_{sk}}{B_m}\right)^2 \left[ \left( \frac{S_w}{B_w} + \frac{S_{\text{CO}_2}}{B_{\text{CO}_2}} + \frac{S_{\text{CH}_4}}{B_{\text{CH}_4}} + \frac{S_{hyd}}{B_{hyd}} \right) \phi + \frac{1-\phi}{B_m} - \frac{B_{sk}}{B_m^2} \right]^{-1} \quad (3)$$

$$\rho_{mix} = \phi(S_w \rho_w + S_{\text{CO}_2} \rho_{\text{CO}_2} + S_{\text{CH}_4} \rho_{\text{CH}_4} + S_{hyd} \rho_{hyd}) + (1-\phi)\rho_m \quad (4)$$

where  $\phi$  is the sediment porosity and  $S$  is the relative saturation with subindices  $w$  for water, CO<sub>2</sub>, CH<sub>4</sub>, and  $hyd$  for hydrate. A similar expression can be used for ice by replacing  $S_{hyd}$ ,  $B_{hyd}$  and  $\rho_{hyd}$  with  $S_{ice}$ ,  $B_{ice}$  and  $\rho_{ice}$ . The physical and mechanical properties of water, CO<sub>2</sub>, CH<sub>4</sub> and solids (i.e., quartz, ice, and hydrate)

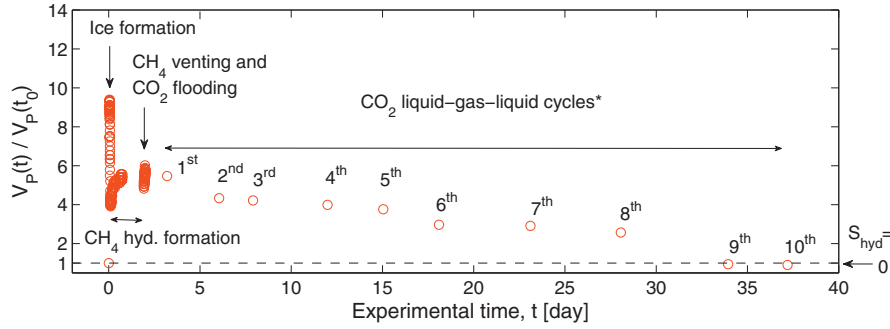


**Fig. 4.** Reduction of hydrate-bearing sand stiffness during successive flushes of pure liquid CO<sub>2</sub>, as liquid–gaseous–liquid CO<sub>2</sub> cycles inside the CH<sub>4</sub> hydrate stability field. The vertical axis represents the ratio between the P-wave velocity at experimental time  $t$  and the initial P-wave velocity at time  $t_0$  before ice and hydrate formation. Each liquid–gas–liquid CO<sub>2</sub> cycle replaces 0.030 kg of pure CO<sub>2</sub> every ~3 days, which is equivalent to 8.5 times the pore space of the sand specimen. Note: (\*) during the CO<sub>2</sub> liquid–gas–liquid cycles, we show the  $V_P$  ratio for the specimen in gas CO<sub>2</sub> to highlight the effect of cementing hydrate on the granular skeleton. The sand does not show any evidence of cementation after the 8th liquid–gas–liquid CO<sub>2</sub> cycle (28th day in the figure).

are summarized in Table 1; notice that the bulk stiffnesses sort as  $B_m > B_{ice} > B_{hyd}$  ( $m$ : mineral). A proper equation of state is used for the fluid phase to account for variations in pressure and temperature (see Table 1).

Eq. (3) disregards the stiffening effect of capillary forces in mixed fluid conditions, such as water–CO<sub>2</sub> mixtures; this approximation is adequate for coarser sediments and/or high effective stress levels. If needed, the value of  $B_{sk}$  can be increased as a function of suction and saturation.

The constrained modulus of the skeleton  $M_{sk}$  can be determined from  $V_P$  measurements in gas saturated sands  $M_{sk} = V_P^2 \rho_{sk}$ . From the theory of elasticity, the bulk and shear modulus of the skeleton are  $B_{sk} = 1/3[(1 + \nu_{sk})/(1 - \nu_{sk})]M_{sk}$  and  $G_{sk} = [(1 - 2\nu_{sk})/(2 - 2\nu_{sk})]M_{sk}$ , where the small strain Poisson's ratio for the granular skeleton is low  $\nu_{sk} = 0.1$  (Santamarina et al., 2001). Knowing  $B_{mix}$  (Eq. (3)),  $G_{sk}$  and  $\rho_{mix}$  (Eq. (4)), the compressive wave velocity of the fluid saturated porous medium can be computed as,

$$V_P = \sqrt{\frac{B_{mix} + (4/3)G_{sk}}{\rho_{mix}}} \quad (5)$$

Fig. 5 shows the ratio  $\beta$  between the P-wave velocity predictions for the sediment saturated with a water–CO<sub>2</sub> mixture ( $S_w + S_{CO_2} = 1$ ), and the same sediment saturated with water only ( $S_w = 1$ ). Values of  $\beta$  are shown as a function of CO<sub>2</sub> saturation for different skeletal stiffnesses  $V_{P,sk}$ , fluid pressures, and porosities. Parameters used in each pane are selected to match the conditions in our experiments and other published studies; data are superimposed on the graphs. The  $\beta$ -ratio is always less than one because the P-wave velocity of liquid CO<sub>2</sub> ranges between ~300 m/s (7 MPa, 300 K) and 590 m/s (10 MPa, 280 K) as compared to that of water  $V_{P,water} \sim 1500$  m/s. The  $\beta$ -ratio is most sensitive to the stiffness of the skeleton  $B_{sk}$  and  $G_{sk}$ , and it tends to  $\beta = 1$  as the stiffness of the skeleton increases. The  $\beta$ -ratio changes significantly with PT conditions and CO<sub>2</sub> saturation  $S_{CO_2}$ . Similar trends apply to brine-saturated media ( $P = 10$  MPa;  $T = 280$  K;  $S = 10\%$ ;  $B_w = 2.11$  GPa;  $B_{brine} = 2.64$  GPa;  $\rho_w = 1004$  kg/m<sup>3</sup>;  $\rho_{brine} = 1075$  kg/m<sup>3</sup>).

An immediate implication of this analysis is that the injection of liquid CO<sub>2</sub> into water-saturated sediment in the field replaces high bulk stiffness water for the more compressible liquid CO<sub>2</sub> and a lower P-wave velocity is anticipated. Also we note that due to the low P-wave velocities of gas CH<sub>4</sub> and both gas and liquid CO<sub>2</sub> compared to the P-wave velocity of the hydrate-bearing sand ( $V_P \sim 900$  m/s at 100 kPa vertical effective stress), P-wave velocities measured in this study closely track the evolution of skeletal stiffness.

While the forward prediction of  $V_P$  is viable, flat trends in Fig. 5 indicate that the estimation of CO<sub>2</sub> saturation from  $V_P$  measurements will be inaccurate, especially in stiff, low porosity sediments where marked changes in CO<sub>2</sub> saturation have almost no impact on  $V_P$ .

### 5.3. Time evolution: formation rate

Diffusion controlled hydrate growth is anticipated at menisci (excess-gas conditions). CH<sub>4</sub> hydrate formation is limited by methane gas transfer through the hydrate layer thickness  $s$  that forms around the menisci (excess-gas sediment). At steady state, the flux of gas  $F_g$  from the pore space (concentration  $C_{bulk}$ ) to the water inside the meniscus (concentration  $C_{aq}$ ) is

$$F_g = D \frac{C_{bulk} - C_{aq}}{s} \quad (6)$$

where  $D$  is the diffusivity of CH<sub>4</sub> through CH<sub>4</sub> hydrate. The concentrations  $C_{bulk} = \rho_{CH_4}$  mol/L and  $C_{aq}$  depend on pressure and temperature conditions (Servio and Englezos, 2002; Servio et al., 1999). The gas concentration in hydrate is  $C_{hyd} = 7.3$  in mol/L (full occupancy  $n = 5.75$ ; lattice size 12 Å). For a quasi cylindrical geometry, the evolution of the hydrate shell thickness in time becomes,

$$s = \sqrt{2D \frac{C_{bulk} - C_{aq}}{C_{hyd} - C_{aq}} t} \quad (7)$$

We estimate the time required for hydrate formation  $t_{form}$  in pendular water at interparticle menisci by combining Eqs. (6) and (7), and substituting  $s$  for  $r_m$ ,

$$t_{form} = \frac{1}{8D} \frac{C_{hyd} - C_{aq}}{C_{bulk} - C_{aq}} d_{50}^2 \sqrt{S_w^{init} e} \quad (8)$$

Experimental diffusion values  $D = 3.4\text{--}7.6 \times 10^{-13}$  m<sup>2</sup>/s (Davies et al., 2008), combined with Eq. (8) lead to the conclusion that water in submillimetric menisci converts to hydrate in few days. Similar rates are expected to happen in diffusion controlled CH<sub>4</sub>–CO<sub>2</sub> replacement processes.

### 5.4. Water solubility in liquid CO<sub>2</sub> and hydrate dissolution

Both CO<sub>2</sub> and CH<sub>4</sub> hydrates tend to dissolve in liquid CO<sub>2</sub> that is not water saturated, as confirmed by the results shown in Fig. 4 (see also Jung et al., 2010). An estimated ~30 mg of water could be dissolved into liquid CO<sub>2</sub> given the void space in our chamber under the experimental conditions in this study. Alternatively, only ~3 mg of water can dissolve into the CO<sub>2</sub>-filled pore space of the sediment cell. The experiment shown in Fig. 4 starts with 180 mg of water in the sediment; i.e.,  $S_w = 0.045$ . Thus, ~180 mg/30 mg = 6 to

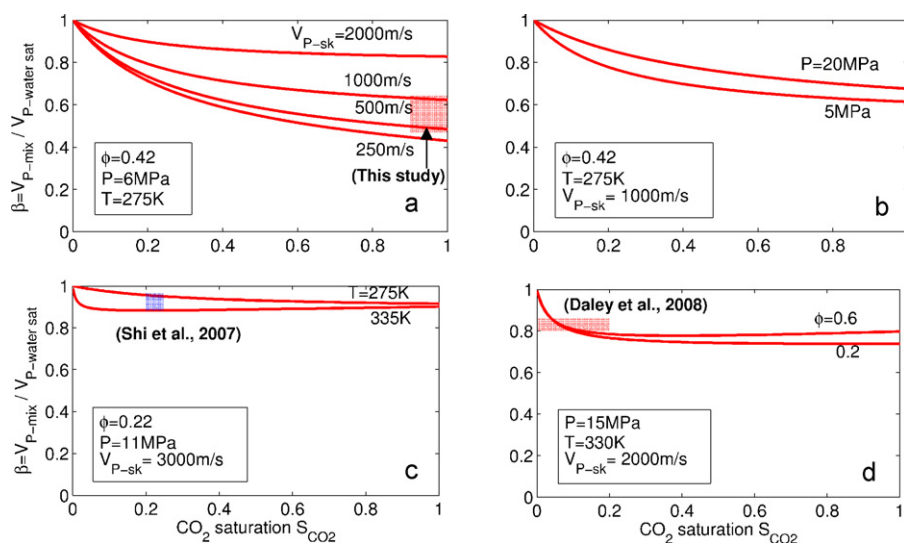


**Fig. 5.** Ratio of compressive P-wave velocities for liquid and supercritical CO<sub>2</sub>–water saturated sediment and the same sediment saturated with water as a function of CO<sub>2</sub> saturation. The effects of (a) skeletal stiffness as represented in  $V_{P-sk}$ ; (b) pore-fluid pressure  $P$ ; (c) temperature  $T$ ; (d) porosity  $\phi$ . The bulk modulus and density of CO<sub>2</sub>, and water are calculated with equations of state as a function of pressure and temperature (Table 1). Laboratory and field results are superimposed.

180 mg/3 mg = 60 flushing cycles of CO<sub>2</sub> are needed to dissolve all hydrate-forming water into the surrounding liquid CO<sub>2</sub>. Nine CO<sub>2</sub> flushing cycles were sufficient in the experiment documented in Fig. 4.

## 6. Conclusions

CH<sub>4</sub>–CO<sub>2</sub> replacement in hydrate-bearing sediments presents a unique opportunity to address increasing energy demands within the context of climate change. Considerable research efforts are needed to understand the complexity of underlying processes leading to commercial scale technological developments.

We designed an experiment that takes advantage of the contact-dependent sand stiffness to follow CH<sub>4</sub> hydrate formation, CO<sub>2</sub> flooding and gas replacement, and subsequent hydrate dissociation. The test design amplifies the process signatures by simultaneously measuring phase reactions that take place at thousands of interparticle menisci.

Hydrate growth in excess-gas sediments is controlled by CH<sub>4</sub> diffusion through the intermediate hydrate shell that separates bulk gas and free water.

After CO<sub>2</sub> flooding, the hydrate mass dissociates at the CO<sub>2</sub> hydrate dissociation boundary, which confirms the successful CH<sub>4</sub>–CO<sub>2</sub> replacement.

The hydrate-bearing sediment retains its stiffness during CO<sub>2</sub> flooding and gas replacement. Therefore, while a lattice-scale solid–liquid–solid transition is required for CH<sub>4</sub>–CO<sub>2</sub> replacement, the reaction is local and does not cause an appreciable effect on the macroscale mechanical properties of the hydrate bearing sediment.

The mutual solubility and diffusivity of water, CO<sub>2</sub>, and CH<sub>4</sub> components play a crucial role in the process of CH<sub>4</sub>–CO<sub>2</sub> replacement. Liquid CO<sub>2</sub> will dry water from the existing hydrate, causing a decrease in both hydrate saturation and sediment stiffness in regions subjected to extensive CO<sub>2</sub> flow, such as near the injection wells. This may lead to volume contraction, trigger borehole instability, and facilitate sand production.

The bulk modulus of CO<sub>2</sub> at reservoir conditions is lower than that of water. Therefore, P-wave velocity decreases as CO<sub>2</sub> displaces water from the pore space. The change in P-wave velocity is small in hard rocks and stiff sediments. This observation limits the use of P-wave monitoring of CO<sub>2</sub> injection.

## Acknowledgments

Support for this research was provided by U.S. Department of Energy. Additional funding was provided by the Goizueta Foundation. C. Barrett carefully edited the manuscript.

## References

- Adisasmito, S., Frank, R.J., Sloan, E.D., 1991. Hydrates of carbon-dioxide and methane mixtures. *Journal of Chemical and Engineering Data* 36, 68–71.
- Anderson, R., Llamado, M., Tohidi, B., Burgass, R.W., 2003. Experimental measurement of methane and carbon dioxide clathrate hydrate equilibria in mesoporous silica. *Journal of Physical Chemistry B* 107, 3507–3514.
- Angeli, M., Soldal, M., Skurtveit, E., Aker, E., 2009. Experimental percolation of supercritical CO<sub>2</sub> through a caprock. *Energy Procedia* 1, 3351–3358.
- Arts, R., Eiken, O., Chadwick, A., Zweigel, P., van der Meer, L., Zinszner, B., 2004. Monitoring of CO<sub>2</sub> injected at Sleipner using time-lapse seismic data. *Energy* 29, 1383–1392.
- Aya, I., Yamane, K., Nariyai, H., 1997. Solubility of CO<sub>2</sub> and density of CO<sub>2</sub> hydrate at 30 MPa. *Energy* 22, 263–271.
- Belogol'skii, V.A., Sekoyan, S.S., Samorukova, L.M., Levtsov, V.I., Stefanov, S.R., 2002. Temperature and pressure dependence of the speed of sound in seawater. *Measurement Techniques* 45, 879–886.
- Bevlins, R.D., 1979. *Formulas for Natural Frequency and Mode Shape*. Krieger Publishing Company, Malabar, Florida.
- Bicher, L.B., Katz, D.L., 1943. Viscosities of the methane–propane system. *Industrial & Engineering Chemistry* 35, 754–761.
- Biot, M.A., 1956. Theory of propagation of elastic waves in a fluid-saturated porous solid: 2. Higher frequency range. *Journal of the Acoustical Society of America* 28, 179–191.
- Bourbie, T., Coussy, O., Zinszner, B., 1987. *Acoustics of Porous Media*. Editions Technip, Paris.
- Cho, G.-C., Dodds, J., Santamarina, J.C., 2006. Particle shape effects on packing density, stiffness, and strength: natural and crushed sands. *Journal of Geotechnical & Geoenvironmental Engineering* 132, 591–602.
- Daley, T.M., Myer, L.R., Peterson, J.E., Majer, E.L., Hoversten, G.M., 2008. Time-lapse crosswell seismic and VSP monitoring of injected CO<sub>2</sub> in a brine aquifer. *Environmental Geology* 54, 1657–1665.
- Davies, S.R., Lachance, J.W., Sloan, E.D., Koh, C.A., 2008. A novel approach to measuring methane diffusivity through a hydrate film using differential scanning calorimetry. In: 6th International Conference on Gas Hydrates, Vancouver, British Columbia, Canada.
- Donnelly, H., Katz, D., 1954. Phase equilibria in the carbon dioxide–methane system. *Industrial and Engineering Chemistry* 46, 511–517.
- Duan, Z.H., Sun, R., 2003. An improved model calculating CO<sub>2</sub> solubility in pure water and aqueous NaCl solutions from 273 to 533 K and from 0 to 2000 bar. *Chemical Geology* 193, 257–271.
- Espinoza, D.N., Santamarina, J.C., 2010. Water–CO<sub>2</sub>–mineral systems: interfacial tension, contact angle and diffusion – implications to CO<sub>2</sub> geological storage. *Water Resources Research* 46, doi:10.1029/2009WR008634.
- Fenghour, A., Wakeham, W.A., Vesovic, V., 1998. The viscosity of carbon dioxide. *Journal of Physical and Chemical Reference Data* 27, 31–44.

- Gueguen, Y., Palciauskas, V., 1994. *Introduction to the Physics of Rocks*. Princeton University Press.
- Hashemi, S., Macchi, A., Bergeron, S., Servio, P., 2006. Prediction of methane and carbon dioxide solubility in water. *Fluid Phase Equilibria* 246, 131–136.
- Helgerud, M.B., Waite, W.F., Kirby, S.H., Nur, A., 2009. Elastic wave speeds and moduli in polycrystalline ice Ih, sl methane hydrate, and slI methane–ethane hydrate. *Journal of Geophysical Research–Solid Earth*, 114.
- Hirohama, S., Shimoyama, Y., Wakabayashi, A., Tatsuta, S., Nishida, N., 1996. Conversion of CH<sub>4</sub>-hydrate to CO<sub>2</sub>-hydrate in liquid CO<sub>2</sub>. *Journal of Chemical Engineering of Japan* 29, 1014–1020.
- James III, W.R., Spyros, K.L., Jerry, M.H., Mark Van, S., 1995. High-resolution crosswell imaging of a west Texas carbonate reservoir: part 3 – wavefield separation of reflections. *Geophysics* 60, 692–701.
- Jung, J., Espinoza, D.N., Santamarina, J.C., 2010. Properties and phenomena relevant to CH<sub>4</sub>–CO<sub>2</sub> replacement in hydrate-bearing sediments. *Journal of Geophysical Research–Solid Earth* 115, B10102, doi:10.1029/2009JB000812.
- Kvamme, B., Graue, A., Buanes, T., Kumetsoua, T., Erslund, G., 2007. Storage of CO<sub>2</sub> in natural gas hydrate reservoirs and the effect of hydrate as an extra sealing in cold aquifers. *International Journal of Greenhouse Gas Control*, 236–246.
- Kvenvolden, K.A., 1988. Methane hydrate – a major reservoir of carbon in the shallow geosphere? *Chemical Geology* 71, 41–51.
- Lee, H., Seo, Y., Seo, Y.T., Moudrakovski, I.L., Ripmeester, J.A., 2003. Recovering methane from solid methane hydrate with carbon dioxide. *Angewandte Chemie-International Edition* 42, 5048–5051.
- Lee, J.S., Santamarina, J.C., 2005. Bender elements: performance and signal interpretation. *Journal of Geotechnical and Geoenvironmental Engineering* 131, 1063–1070.
- Lei, X.L., Xue, Z.Q., 2009. Ultrasonic velocity and attenuation during CO<sub>2</sub> injection into water-saturated porous sandstone: measurements using difference seismic tomography. *Physics of the Earth and Planetary Interiors* 176, 224–234.
- Mavko, G., Mukerji, T., Dvorkin, J., 2009. *The Rock Physics Handbook. Tools for Seismic Analysis of Porous Media*, second ed. Cambridge University Press, New York.
- McGrail, B.P., Schaefer, H.T., White, M.D., Zhu, T., Kulkarni, A.S., Hunter, R.B., Patil, S.L., Owen, A.T., Martin, P.F., 2007. Using Carbon Dioxide to Enhance Recovery of Methane from Gas Hydrate Reservoirs: Final Summary Report. PNNL-17035. Pacific Northwest National Laboratory operated by Battelle Memorial Institute for the U.S. Department of Energy, Oak Ridge, TN.
- Netherton, R., Piwinski, A.J., Chan, M., 1977. Viscosity of brine from Salton sea geothermal field, California, from 25 °C to 90 °C at 100 kPa. *Transactions-American Geophysical Union* 58, 1248–1248.
- NIST, 2010. Scientific and technical databases – thermophysical and thermochemical.
- Peng, D., Robinson, D.B., 1976. New 2-constant equation of state. *Industrial & Engineering Chemistry Fundamentals* 15, 59–64.
- Poulos, H.G., Davis, E.H., 1974. *Elastic Solutions for Soil and Rock Mechanics*. Wiley.
- Santamarina, J.C., Klein, K.A., Fam, M.A., 2001. *Soils and Waves*. Wiley.
- Sarout, J., Piane, C.D., Dewhurst, D., 2009. Elastic Properties of a Mixed Shale/Sandstone Specimen Simulating Reservoir/Cap–Rock Interface, 8th Euro-conference of Rock Physics and Geomechanics. Ascona, Switzerland.
- Seo, Y.T., Lee, H., 2001. Multiple-phase hydrate equilibria of the ternary carbon dioxide, methane, and water mixtures. *Journal of Physical Chemistry B* 105, 10084–10090.
- Servio, P., Englezos, P., 2001. Effect of temperature and pressure on the solubility of carbon dioxide in water in the presence of gas hydrate. *Fluid Phase Equilibria* 190, 127–134.
- Servio, P., Englezos, P., 2002. Measurement of dissolved methane in water in equilibrium with its hydrate. *Journal of Chemical and Engineering Data* 47, 87–90.
- Servio, P., Lagers, F., Peters, C., Englezos, P., 1999. Gas hydrate phase equilibrium in the system methane–carbon dioxide–neohexane and water. *Fluid Phase Equilibria* 158, 795–800.
- Shi, J.Q., Xue, Z.Q., Durucan, S., 2007. Seismic monitoring and modelling of supercritical CO<sub>2</sub> injection into a water-saturated sandstone: interpretation of P-wave velocity data. *International Journal of Greenhouse Gas Control* 1, 473–480.
- Sloan, E.D., Koh, C.A., 2008. *Clathrate Hydrates of Natural Gases*, third ed. CRC Press, Boca Raton, FL.
- Span, R., Wagner, W., 1996. A new equation of state for carbon dioxide covering the fluid region from the triple-point temperature to 1100 K at pressures up to 800 MPa. *Journal of Physical and Chemical Reference Data* 25, 1509–1596.
- Spycher, N., Pruess, K., Ennis-King, J., 2003. CO<sub>2</sub>–H<sub>2</sub>O mixtures in the geological sequestration of CO<sub>2</sub>. I. Assessment and calculation of mutual solubilities from 12 to 100 °C and up to 600 bar. *Geochimica et Cosmochimica Acta* 67, 3015–3031.
- Spyros, K.L., Bruce, P.M., 1997. Crosswell seismic imaging of reservoir changes caused by CO<sub>2</sub> injection. *The Leading Edge* 16, 1300–1308.
- Spyros, K.L., Jerry, M.H., James III, W.R., Mark Van, S., 1995. High-resolution crosswell imaging of a west Texas carbonate reservoir: part 4 – reflection imaging. *Geophysics* 60, 702–711.
- Tegze, G., Granasy, L., Kvamme, B., 2007. Phase field modeling of CH<sub>4</sub> hydrate conversion into CO<sub>2</sub> hydrate in the presence of liquid CO<sub>2</sub>. *Physical Chemistry Chemical Physics* 9, 3104–3111.
- Trusler, J.P.M., Zarari, M., 1992. The speed of sound and derived thermodynamic properties of methane at temperatures between 275-K and 375-K and pressures up to 10-MPa. *Journal of Chemical Thermodynamics* 24, 973–991.
- Vesovic, V., Wakeham, W.A., Olchoway, G.A., Sengers, J.V., Watson, J.T.R., Millat, J., 1990. The transport-properties of carbon-dioxide. *Journal of Physical and Chemical Reference Data* 19, 763–808.
- Waite, W.F., Santamarina, J.C., Cortes, D.D., Dugan, B., Espinoza, D.N., Germaine, J., Jang, J., Jung, J., Kneafsey, T., Shin, H.S., Soga, K., Winters, W.J., Yun, T.-S., 2009. Physical properties of hydrate-bearing sediments. *Reviews of Geophysics* 47, RG4003, doi:10.1029/2008RG000279.
- Xue, Z., Tanase, D., Watanabe, J., 2006. Estimation of CO<sub>2</sub> saturation from time-lapse CO<sub>2</sub> well logging in an onshore aquifer, Nagaoka, Japan. *Exploration Geophysics* 37, 19–29, doi:10.1071/EG06019.